


# Considerations for hyperpolarized 13C MR at reduced field: Comparing 1.5T versus 3T

**Journal Article****Author(s):**

Traechtler, Julia; Fuetterer, Maximilian; [Albannay, Mohammed](#) ; Hoh, Tobias; Kozerke, Sebastian

**Publication date:**

2023-05

**Permanent link:**

<https://doi.org/10.3929/ethz-b-000592820>

**Rights / license:**

[Creative Commons Attribution-NonCommercial-NoDerivatives 4.0 International](#)

**Originally published in:**

Magnetic Resonance in Medicine 89(5), <https://doi.org/10.1002/mrm.29579>

**Funding acknowledgement:**

820374 - Leveraging room temperature diamond quantum dynamics to enable safe, first-of-its-kind, multimodal cardiac imaging (EC)

# Considerations for hyperpolarized $^{13}\text{C}$ MR at reduced field: Comparing 1.5T versus 3T

Julia Traechtler<sup>1</sup> | Maximilian Fuetterer<sup>1</sup> | Mohammed M. Albannay<sup>1,2</sup> | Tobias Hoh<sup>1</sup> | Sebastian Kozerke<sup>1</sup>

<sup>1</sup>Institute for Biomedical Engineering, University and ETH Zurich, Zurich, Switzerland

<sup>2</sup>Laboratory of Physical Chemistry, ETH Zurich, Zurich, Switzerland

## Correspondence

Sebastian Kozerke, Institute for Biomedical Engineering, University and ETH Zurich, Gloriastrasse 35, 8092 Zurich, Switzerland.  
Email: kozerke@biomed.ee.ethz.ch

## Funding information

Horizon 2020 FETFLAG MetaboliQs, Grant/Award Number: Grant/Award Number: 820374; Maexi Foundation (Zurich, Switzerland) Project: CMRPredict

**Purpose:** In contrast to conventional MR, signal-to-noise ratio (SNR) is not linearly dependent on field strength in hyperpolarized MR, as polarization is generated outside the MR system. Moreover, field inhomogeneity-induced artifacts and other practical limitations associated with field strengths  $\geq 3\text{T}$  are alleviated at lower fields. The potential of hyperpolarized  $^{13}\text{C}$  spectroscopy and imaging at 1.5T versus 3T is demonstrated in silico, in vitro, and in vivo for applications on clinical MR systems.

**Theory and Methods:** Theoretical noise and SNR behavior at different field strengths are investigated based on simulations. A thorough field comparison between 1.5T and 3T is performed using thermal and hyperpolarized  $^{13}\text{C}$  spectroscopy and imaging. Cardiac in vivo data is obtained in pigs using hyperpolarized  $[1-^{13}\text{C}]$ pyruvate spectroscopy and imaging at 1.5T and 3T.

**Results:** Based on theoretical considerations and simulations, the SNR of hyperpolarized MR at identical acquisition bandwidths is independent of the field strength for typical coil setups, while adaptively changing the acquisition bandwidth proportional to the static magnetic field allows for net SNR gains of up to 40% at 1.5T compared to 3T. In vitro  $^{13}\text{C}$  data verified these considerations with less than 7% deviation. In vivo feasibility of hyperpolarized  $[1-^{13}\text{C}]$ pyruvate dynamic metabolic spectroscopy and imaging at 1.5T is demonstrated in the pig heart with comparable SNR between 1.5T and 3T while  $B_0$  artifacts are noticeably reduced at 1.5T.

**Conclusion:** Hyperpolarized  $^{13}\text{C}$  MR at lower field strengths is favorable in terms of SNR and off-resonance effects, which makes 1.5T a promising alternative to 3T, especially for clinical cardiac metabolic imaging.

## KEYWORDS

1.5T versus 3T, field comparison, field inhomogeneities, hyperpolarized  $^{13}\text{C}$ , signal-to-noise ratio

## 1 | INTRODUCTION

Hyperpolarized  $^{13}\text{C}$  MRI and MR spectroscopy (MRS) are used for monitoring real-time metabolism in vivo.<sup>1-3</sup>

Typically, in vivo hyperpolarized  $^{13}\text{C}$  MRI/MRS are performed at field strengths  $\geq 3\text{T}$ . Especially clinical examinations and preclinical studies in large animals are usually conducted at  $3\text{T}^1$  due to commercially available hardware suitable for the respective subject sizes with the capability of detecting non- $^1\text{H}$  nuclei.

In the classical MR signal-to-noise ratio (SNR) paradigm, higher field equals higher SNR. In hyperpolarized MR, however, lower field strengths can be favorable in larger subjects such as humans and pigs, with a higher theoretical SNR for typical coil sizes and loading conditions.<sup>4</sup> Moreover, reduced static magnetic fields alleviate frequent challenges related to susceptibility effects,<sup>5-7</sup> field inhomogeneities, patient exposure (specific absorption rate),<sup>4</sup> and other constraints as mentioned in the following.

Various works in hyperpolarized MR address off-resonance-induced imaging artifacts such as geometric distortions, blurring, and local signal dephasing.<sup>8-16</sup> As field inhomogeneities are proportional to the static magnetic field, data acquisition at lower field strengths is less prone to off-resonance-related artifacts, and thus, improved image quality can be achieved.

In-bore electrocardiogram (ECG) signals are commonly derived to synchronize acquisitions with the subject's heartbeat, either to account for intra-beat motion and pulsatile flow, or to serve as reference for bolus dynamics in case of (hyperpolarized) contrast agents. In the MR environment, the ECG signal is corrupted by the field-dependent magnetohydrodynamic effect,<sup>17</sup> posing additional practical challenges to examinations at higher field strengths. As unreliable ECG triggering can render an examination unusable, this is of particular interest to (hyperpolarized) MR with contrast agent administration, where scans cannot easily be repeated.

The above-mentioned considerations have led to the majority of clinical  $^1\text{H}$  cardiovascular MR examinations being performed at  $1.5\text{T}$  rather than  $3\text{T}$ ,<sup>18</sup> and hence, integration of hyperpolarized MR into existing clinical protocols is not straightforward. Adopting a moderate field strength of  $1.5\text{T}$  is therefore considered an important step toward clinical translation of hyperpolarized cardiovascular MR in a multimodal context.

Consequently, this work examines the potential of hyperpolarized  $^{13}\text{C}$  MRS and MRI at the clinically established field strength of  $1.5\text{T}$  with the focus on cardiac applications. Based on theoretical considerations and simulations, SNR performance of hyperpolarized  $^{13}\text{C}$  MR

at field strengths  $\leq 3\text{T}$  is investigated. Furthermore, an extensive field comparison between  $1.5\text{T}$  and  $3\text{T}$  using  $^{13}\text{C}$  MRS and MRI is performed on thermally polarized phantom and hyperpolarized in vitro data. Feasibility and suitability of in vivo hyperpolarized [ $1\text{-}^{13}\text{C}$ ]pyruvate dynamic metabolic MRS and MRI at  $1.5\text{T}$  is explored in a pig model.

## 2 | THEORY

### 2.1 | Noise and SNR

Intrinsic MR SNR is defined as the ratio of the MR signal  $S$  at spatial location  $\vec{x}$ , and noise  $\sigma_{\text{meas}}$  caused by random thermal fluctuations in the measured signal:<sup>19</sup>

$$\text{SNR}(\vec{x}) = \frac{S(\vec{x})}{\sigma_{\text{meas}}}. \quad (1)$$

Field strength dependency of both the signal and noise<sup>4</sup> are elaborated in the following.

The MR signal can be described as a function of transverse magnetization  $M_{xy}$ , coil sensitivity  $C$  and Larmor frequency  $\omega = \gamma B_0$  with  $\gamma$  denoting the gyromagnetic ratio and  $B_0$  the static magnetic field:

$$S(\vec{x}) \propto \omega \cdot M_{xy}(\vec{x}) \cdot C(\vec{x}). \quad (2)$$

Transverse magnetization is proportional to longitudinal magnetization which scales linearly with the polarization  $P$ :<sup>19</sup>

$$P \stackrel{\text{thermal}}{=} \tanh\left(\frac{\gamma \hbar B_0}{2k_B T}\right) \approx \frac{\gamma \hbar B_0}{2k_B T} \stackrel{B_0 \propto \omega}{\propto} \omega, \quad (3)$$

where  $\hbar$  is the reduced Planck constant,  $k_B$  the Boltzmann constant and  $T$  the temperature. For hyperpolarized MR signals, polarization is generated inside the polarizer rather than by the static magnetic field of the MR scanner, and therefore, transverse magnetization is independent of  $B_0$ <sup>20</sup> when neglecting relaxation and radio frequency (RF) excitation. Consequently, in contrast to conventional MR, hyperpolarized signal field dependency arises only from Faraday induction. Therefore, the detectable hyperpolarized signal scales linearly rather than quadratically with  $\omega$ :

$$S(\vec{x}) \stackrel{M_{xy} \propto P}{\propto} \omega \cdot P \propto \begin{cases} \omega^2, & \text{thermal polarization} \\ \omega, & \text{hyperpolarization.} \end{cases} \quad (4)$$

The overall measured noise  $\sigma_{\text{meas}}$  results from thermal fluctuations in the coil  $\sigma_c$ , sample  $\sigma_s$  and electronic system

$\sigma_e$  comprising noise contributions of the matching network and the preamplifier, which can be represented by a series of equivalent resistances  $R_i$ :<sup>19</sup>

$$\sigma_{\text{meas}} = \sqrt{4k_B(T_c R_c + T_s R_s + T_e R_e) \cdot \text{BW}}, \quad (5)$$

where  $T_i$  denote the corresponding temperatures and BW the acquisition bandwidth. While coil and sample noise experience a physical field dependency, electronic system noise is assumed to be field- and frequency-independent for the relevant range of frequencies, and hence neglected in the following. For a single-loop receive coil with radius  $r$ , made of a wire of radial thickness (radius)  $p$  with electrical resistivity  $\rho$ , and loaded with an ideal sample of conductivity  $\kappa$  at distance  $d$  (Figure S1) and  $\mu_0$  being the vacuum permeability, the equivalent coil and sample resistances can be expressed as:<sup>21-23</sup>

$$R_c = \frac{r}{p} \sqrt{\frac{\mu_0 \omega \rho}{2}}$$

$$R_s = \frac{2}{3\pi} \kappa \mu_0^2 \omega^2 r^3 \arctan\left(\frac{\pi r}{8d}\right), \quad (6)$$

which yields the following frequency and bandwidth dependencies of the corresponding noise contributions:

$$\sigma_c = \sqrt{4k_B T_c R_c \text{BW}} \propto \sqrt{\omega^{0.5} \cdot \text{BW}}$$

$$\sigma_s = \sqrt{4k_B T_s R_s \text{BW}} \propto \sqrt{\omega^2 \cdot \text{BW}}. \quad (7)$$

By combining Equations (1)–(7), the SNR scaling of hyperpolarized MR follows:<sup>24,25</sup>

$$\text{SNR}(\vec{x}) \propto \frac{\omega \cdot M_{xy}(\vec{x}) \cdot C(\vec{x})}{\sqrt{4k_B(T_c R_c + T_s R_s + T_e R_e) \cdot \text{BW}}}$$

$$\stackrel{\text{hyperpol.}}{\propto} \frac{\omega}{\sqrt{(\omega^{0.5} + \omega^2) \cdot \text{BW}}}. \quad (8)$$

Depending on coil and loading characteristics, two field-dependent noise regimes can be distinguished for SNR scaling, in which either  $R_c$  or  $R_s$  dominates. For small coil diameters, coil noise dominates over sample noise ( $R_c \gg R_s$ ), leading to an SNR that increases with field strength:

$$\text{SNR}_{R_c \gg R_s} \propto \frac{\omega}{\sqrt{\omega^{0.5} \cdot \text{BW}}} = \frac{\omega^{\frac{3}{4}}}{\sqrt{\text{BW}}}, \quad (9)$$

whereas in the sample noise-dominated regime ( $R_s \gg R_c$ ), SNR becomes field-independent and solely dependent on

the acquisition bandwidth for fixed coil and loading characteristics:

$$\text{SNR}_{R_s \gg R_c} \propto \frac{\omega}{\sqrt{\omega^2 \cdot \text{BW}}} = \frac{1}{\sqrt{\text{BW}}}. \quad (10)$$

The noise regime for a given single-loop experimental setup is determined by the loss mechanisms in the receive coil, which are quantified by the quality factor (Q-factor)  $Q$ . Experimentally, the noise regime can be verified based on the ratio of unloaded  $Q_u$  to loaded  $Q_l$ :

$$Q_{\text{ratio}} = \frac{Q_u}{Q_l} = \frac{R_c + R_s}{R_c}, \quad (11)$$

where sample noise exceeds coil noise ( $R_s > R_c$ ) whenever the Q-ratio is above two ( $Q_{\text{ratio}} > 2$ ).

## 2.2 | Bandwidth adaption

Under the assumption of very long transverse relaxation times  $T_2$  for hyperpolarized substrates,  $T_2^*$  decay is dominated by field inhomogeneities  $(\gamma/2\pi)\Delta B_0$  which depend on  $\omega$ :

$$\frac{1}{T_2^*} = \frac{1}{T_2} + (\gamma/2\pi)\Delta B_0 \xrightarrow{T_2 \text{ long}} T_2^* \propto \frac{1}{\omega}. \quad (12)$$

Hence, as  $T_2^*$  increases at lower field strengths, the available signal persists longer, which, together with the reduced spectral span of the metabolites at lower fields, can be utilized to adaptively change the acquisition bandwidth proportional to  $\omega$ , that is,  $\text{BW} \propto \omega$ . For the field-dependent SNR scaling according to Equations (9) and (10) follows:

$$\text{SNR}_{R_c \gg R_s} \stackrel{\text{adapt. BW}}{\propto} \frac{\omega^{\frac{3}{4}}}{\sqrt{\omega}} = \omega^{\frac{1}{4}}$$

$$\text{SNR}_{R_s \gg R_c} \stackrel{\text{adapt. BW}}{\propto} \frac{1}{\sqrt{\omega}} = \omega^{-\frac{1}{2}}. \quad (13)$$

Hence, the effective SNR scaling favors lower field strengths in the sample noise-dominated regime.

## 3 | METHODS

To validate the theoretical SNR considerations from the previous section, Q-ratio and relaxometry measurements followed by simulation, thermal phantom, hyperpolarized in vitro and in vivo experiments are presented as depicted in Figure 1.

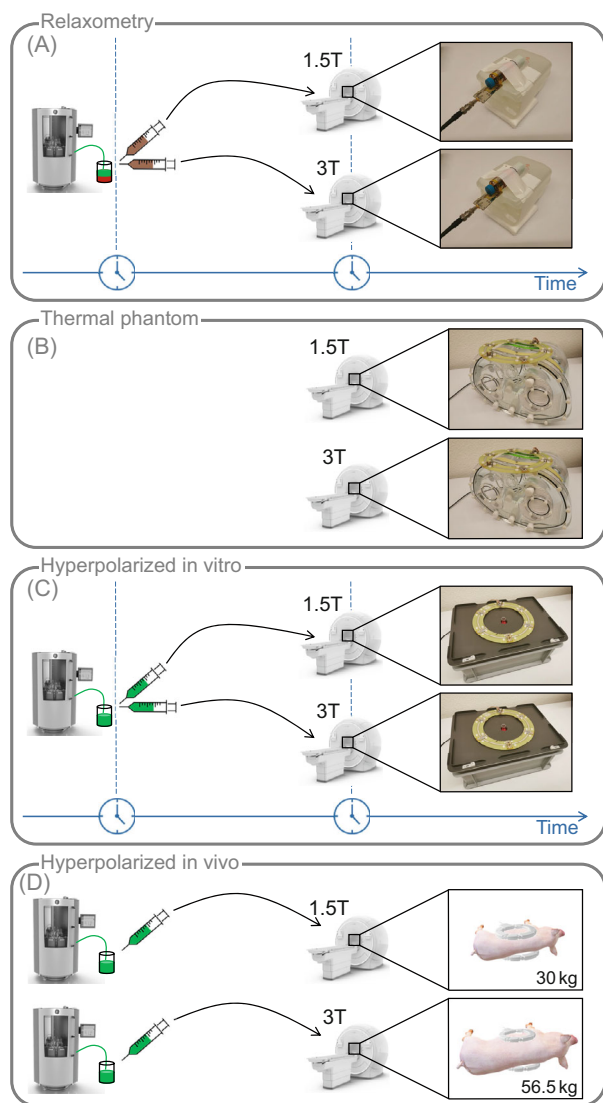


**FIGURE 1** Overview of the experimental methods presented in this work. Simultaneous dissolutions and measurements at 1.5T and 3T are depicted in blue. (A) In vitro  $T_2$  and  $T_1$  relaxometry experiments of hyperpolarized  $^{13}\text{C}$  pyruvate in blood (Section 3.2). (B) Field comparison experiments using a thermal  $^{13}\text{C}$  urea torso phantom (Section 3.4). (C) In vitro field comparison experiments using hyperpolarized  $^{13}\text{C}$  pyruvate (Section 3.5). (D) Metabolic in vivo measurements using hyperpolarized  $^{13}\text{C}$  pyruvate in the pig heart (Section 3.6)

Relaxometry, phantom, in vitro, and in vivo field comparison experiments were performed on clinical 1.5T and 3T scanners (Achieva / Ingenia; Philips Healthcare) equipped with identical transmit-receive RF chains including identical integrated preamplifiers, and using geometrically identical coils tuned to 16 and 32 MHz, respectively. Loop sizes were fixed between field strengths for anatomical reasons assuming an optimal geometry for the target organ (heart). Sequence parameters are listed in Table 1. For hyperpolarization,  $[1-^{13}\text{C}]$ pyruvic acid doped with 15 mM trityl radical was polarized to  $>40\%$

in a commercial SpinLab hyperpolarizer (General Electric Healthcare) and dissolved in neutralization media yielding 250 mM  $[1-^{13}\text{C}]$ pyruvate solution.

An overview of the applied coils and experimental setups can be found in Figures S2 and S3.

Data reconstruction and quantification were performed in MATLAB (MathWorks).

### 3.1 | Q-ratio measurements

To determine the noise regime, Q-ratio measurements were performed with two (16.06 and 32.12 MHz) geometrically identical in-house built  $^{13}\text{C}$  single-loop coils ( $r = 10$  cm) using the dual probe method<sup>26</sup> (two geometrically decoupled pick-up coils,  $r = 1.15$  cm, Figure S2A) and using an E5071C network analyzer (Agilent Technologies). The Q-ratio was determined for various loads with the single-loop coil placed at varying distances ranging from 5 to 110 mm between the conductive coil structures and the subject's chest (Figures S3A and S4).

### 3.2 | Relaxometry experiments in vitro

To examine the field dependency of relaxation times,  $T_2$  and  $T_1$  values of hyperpolarized  $[1-^{13}\text{C}]$ pyruvate in blood were determined in vitro using  $^{13}\text{C}$  MRS at 1.5T and 3T.

Relaxation parameters were measured simultaneously on 1.5T and 3T scanners using geometrically identical in-house built  $^{13}\text{C}$  transmit-receive volume saddle coils ( $r = 1.5$  cm, length = 10 cm, Figures S2B and S3B). For each measurement, 250 mM neutralized hyperpolarized  $[1-^{13}\text{C}]$ pyruvate solution was dissolved in fresh venous pig blood to achieve concentrations between 12.5 and 250 mM (neat). The pyruvate-blood mixtures were then divided into two samples to ensure consistent polarization and concentration between measurements at both field strengths. All experiments related to blood samples were approved by the Cantonal Veterinary Office.

$T_2$  relaxation was acquired using a custom slice-selective Carr-Purcell-Meibloom-Gill (CPMG) sequence<sup>27</sup> (30 mm slice thickness) with 1024 echoes and an echo-spacing of 10 ms.  $T_2$  relaxation times were obtained as the average from the even and odd echoes' monoexponential fit of the spectral maxima.

$T_1$  relaxation was determined using dynamic slice-selective pulse-acquire spectroscopy ( $5^\circ$  flip angle, 25 mm slice thickness) with 10 acquisitions separated by 10 s.  $T_1$  relaxation times  $T_1$  were fitted monoexponentially from the averaged first three free induction decay (FID) samples according to:  $\exp(-t/T_1) \cdot \cos(5^\circ)^{n-1}$  with  $t = [0, 10, \dots, 90]$  s and  $n = [1, 2, \dots, 10]$ .

**TABLE 1** Sequence parameters for hyperpolarized <sup>13</sup>C spectroscopy and imaging of the thermal phantom, in vitro and in vivo experiments

|   | Thermal phantom<br>(Section 3.4) | Hyperpolarization in vitro<br>(Section 3.5) | Hyperpolarization in vivo<br>(Section 3.6) |
|---|----------------------------------|---|--|
| <b>Slice- and Nonselective spectroscopy</b>             |                                  |   |  |
| Flip angle  | 90°                              | 10°   | 10°  |
| Slice thickness <sup>1</sup>                            | 300 mm                           | 30 mm                                       | 30 mm                                      |
| Averages  | 128                              | 1   | 1  |
| Dynamics  | 1                                | 1   | 120  |
| Acquisition bandwidth (full)                            | 32 kHz                           | 32 kHz                                      | 32 kHz                                     |
| Retrospectively reduced                                 | 16 kHz                           | 16 kHz                                      |  |
| <b>Spiral and EPI imaging</b>                           |                                  |   |  |
| Flip angle  | 30°                              | 30°   | 30° (SPSP)                                 |
| Field of view   | 220×220 mm <sup>2</sup>          | 100×100 mm <sup>2</sup>                     | 220×220 mm <sup>2</sup>                    |
| In-plane resolution                                     | 5×5 mm <sup>2</sup>              | 3×3 mm <sup>2</sup>                         | 5×5 mm <sup>2</sup>                        |
| Reconstruction resolution                               | 1×1 mm <sup>2</sup>              | 1×1 mm <sup>2</sup>                         | 1×1 mm <sup>2</sup>                        |
| Slice thickness   | 30 mm                            | 30 mm                                       | 30 mm                                      |
| Averages  | 128                              | 1   | 1  |
| Dynamics  | 1                                | 1   | 25   |
| Interleaves <sup>2</sup>                                | 1                                | 1   |  |
| Partial Fourier factor <sup>3</sup>                     | 0.75                             | 1.0   | 0.75                                       |
| Spiral acquisition window 1.5T / 3T (full) <sup>2</sup> | 26.4 ms / 26.4 ms                | 26.3 ms / 33.5 ms                           |  |
| Reduced   | 44.2 ms / 44.2 ms                |   |  |
| EPI bandwidth 1.5T / 3T (full) <sup>3</sup>             | 1600 Hz / 1600 Hz                | 1000 Hz / 750 Hz                            | 1600 Hz / 1100 Hz                          |
| Reduced   | 800 Hz / 800 Hz                  |   |  |

Abbreviations: EPI, echo-planar imaging; SPSP, spectral-spatial.

<sup>1</sup>For slice-selective spectroscopy only.

<sup>2</sup>For spiral imaging only.

<sup>3</sup>For EPI only.

To investigate the impact of T<sub>1</sub> relaxation-induced signal loss on the SNR field comparison, a simple two-stage bolus timing model<sup>28</sup> (Figure S6) was implemented in MATLAB to simulate the SNR loss due to longitudinal relaxation of hyperpolarized pyruvate prior to injection (stage 1, neat pyruvate) and postinjection until myocardial bolus peak (stage 2, varying pyruvate-blood concentrations). The model was parameterized based on the experimentally determined T<sub>1</sub> relaxation times at 1.5T and 3T, respectively.

### 3.3 | Computer simulations

Based on the theoretical elaborations from Section 2, noise resistance values, absolute noise levels, and intrinsic SNR of a hyperpolarized <sup>13</sup>C MR signal using fixed and adaptive acquisition bandwidth were simulated in MATLAB to analyze SNR performance at different field strengths.

Theoretical noise behavior was investigated for field strengths B<sub>0</sub> between 0.5T and 3.5T and for coil radii of r = 2.5, 5, 10 cm representing a range of target anatomies. Based on that, the corresponding relative SNR scaling was simulated for fixed and adaptive acquisition bandwidth, and for target depths (distance of the coil to the target organ) of l = 5, 7.5, 10 cm. For the noise resistance values according to Equation (6), a single-looped copper coil with p = 0.5 mm wire thickness (radius) and ρ = 1.77 · 10<sup>-8</sup> Ωm<sup>29</sup> was simulated at a distance d = 1 cm to a semi-infinite conducting sample of muscle (Figure S1). Noise contributions according to Equation (7) were simulated for coil and sample temperatures of T<sub>c</sub> = 300 K, T<sub>s</sub> = 310 K, and an acquisition bandwidth of BW = 32 kHz. For the final SNR scaling as stated in Equation (8), coil sensitivities were simulated according to the Biot-Savart law with a signal point source. Noise figures of preamplifiers and other receive chain components were considered constant.

Synthetic spectra of hyperpolarized [ $1\text{-}^{13}\text{C}$ ]pyruvate with downstream metabolites lactate, pyruvate hydrate, alanine, and bicarbonate were simulated with fixed and adaptive acquisition bandwidth based on the intrinsic SNR calculations. Using the experimentally determined  $T_2$  values for a realistic in vivo pyruvate concentration in blood (12.5 mM) (Section 3.2), field-dependent scaling of  $T_2^*$  was simulated according to Equation (12). The amplitudes of the individual metabolites were scaled in a qualitative manner to represent an exemplary  $^{13}\text{C}$  spectrum.

### 3.4 | Thermal phantom experiments

Using thermal  $^{13}\text{C}$  urea spectroscopy and imaging, a field comparison between 1.5T and 3T with respect to SNR and field inhomogeneity effects was performed on an anthropomorphic torso phantom (SPECT; Supertech) containing a saline solution ( $\kappa \approx 0.6\text{ S/m}$ ) in the main part of the torso, and a myocardial compartment filled with gadolinium-enriched thermal (nonhyperpolarized)  $^{13}\text{C}$  urea ( $\sim 4.5\text{ M}$ ) (Figure S3C).

Measurements were conducted on clinical 1.5T and 3T scanners with geometrically identical in-house built single-loop ( $r = 10\text{ cm}$ )  $^{13}\text{C}$  transmit-receive coils (Figure S2C).

Spectroscopic data were acquired using slice-selective and nonselective pulse-acquire spectroscopy with fixed acquisition bandwidth. Spectral SNR was calculated in the time domain as the FID magnitude over acquisition time  $t_{\text{acq}}$  divided by the standard deviation (SD) of the noise tail (200 samples)  $\text{FID}_{\text{noise}}$ , and spectral peak SNR (pSNR) was determined from the maximum spectral SNR:

$$\begin{aligned} \text{spectral SNR}(t_{\text{acq}}) &= \frac{|\text{FID}(t_{\text{acq}})|}{\text{SD}(\text{Re}\{\text{FID}_{\text{noise}}\})} \\ \text{spectral pSNR} &= \max_{t_{\text{acq}}} \{\text{SNR}(t_{\text{acq}})\}. \end{aligned} \quad (14)$$

Imaging was performed with spiral and echo-planar imaging (EPI) readouts with fixed and adaptive acquisition bandwidth. Image SNR was calculated as the magnitude of the image  $\rho$  over pixels  $v$  divided by the SD over all k-space samples of a separate noise scan  $\text{ksp}_{\text{noise}}$  acquired without RF excitation and gradients, and image pSNR was determined from the 10 pixels with highest intensity (max10):

$$\begin{aligned} \text{image SNR}(v) &= \frac{|\rho(v)|}{\text{SD}(\text{Re}\{\text{ksp}_{\text{noise}}\})} \\ \text{image pSNR} &= \frac{1}{10} \sum_{i=1}^{10} \max_v \{\text{SNR}(v)\}. \end{aligned} \quad (15)$$

### 3.5 | Hyperpolarized in vitro experiments

In addition to the thermal phantom experiments, an in vitro field comparison between 1.5T and 3T was performed for hyperpolarized  $^{13}\text{C}$  pyruvate spectroscopy and imaging.

250 mM neutralized [ $1\text{-}^{13}\text{C}$ ]pyruvate solution was injected approximately 30 s after dissolution into test tubes embedded into boxes filled with a TX151 solidifying powder-water mixture ( $\kappa \approx 0.8\text{ S/m}$ ) as illustrated in Figure S3D. For each dissolution, slice-selective spectroscopy, nonselective spectroscopy, as well as spiral and EPI images were acquired consecutively. Data acquisition was synchronized between 1.5T and 3T scanners using the same hyperpolarized pyruvate solution and geometrically identical in-house built single-loop ( $r = 10\text{ cm}$ )  $^{13}\text{C}$  transmit-receive coils (Figure S2C).

Spectroscopic data were acquired using slice-selective and nonselective pulse-acquire spectroscopy with fixed acquisition bandwidth. Spectral SNR and pSNR were determined according to Equation (14).

Imaging was performed with spiral and EPI readouts with fixed acquisition bandwidth. Image SNR and pSNR were determined according to Equation (15).

### 3.6 | Hyperpolarized in vivo experiments

In vivo data were acquired in anesthetized healthy female pigs (Swiss Large White “Edelschwein”) on clinical 1.5T and 3T systems with geometrically identical dual-loop ( $r = 10\text{ cm}$ )  $^{13}\text{C}$  transmit-receive Helmholtz-like surface coils (PulseTeq; Chobham) (Figure S2D). For each measurement, 0.7 ml/kg of 250 mM neutralized hyperpolarized [ $1\text{-}^{13}\text{C}$ ]pyruvate solution were injected approximately 20 s postdissolution over  $\sim 10\text{ s}$  into the femoral vein. Two injections following dynamic metabolic spectroscopy or imaging, respectively, were performed per animal. Dynamic data were acquired during suspended ventilation using cardiac synchronization and triggering based on ECG at 1.5T, and peripheral pulse unit (PPU) at 3T due to a poor ECG signal. All experiments were performed in accordance with the Swiss Animal Protection Law and Ordinance.

Spectroscopic data were acquired using slice-selective pulse-acquire spectroscopy with fixed acquisition bandwidth. Spectral SNR was calculated in the time domain from the maximum FID magnitude and the standard deviation of the noise tail (200 samples) for each dynamic frame separately, yielding the SNR time curve for the total carbon signal (lactate, pyruvate hydrate, alanine, pyruvate, and bicarbonate). The area under the curve (AUC) was

calculated by signal integration of the total carbon SNR over peak dynamic scan time.

Metabolic images were obtained using echo shift encoding over two consecutive heartbeats with six echo-shifted images (12.3/11.6 ms echo time and 2.3/1.15 ms echo spacing at 1.5T/3T) acquired with a spectrally selective binomial 1-2-1 excitation pulse (30° flip angle, 20 ppm excitation bandwidth), interleaved by a pyruvate shot acquired with a sinc pulse (5° flip angle, 0.75 ms duration).<sup>10,30</sup> Reconstruction was performed in MATLAB using nonlinear conjugate gradient-based reconstruction with ground truth  $B_0$  correction based on a measured  $^1\text{H}$  field map, and total variation regularization with  $\lambda = 0.3$ .<sup>10</sup> Image SNR was calculated as the magnitude of the metabolite ( $m$ ) image  $\rho_m$  over pixels  $v$  of each dynamic frame  $t_d$  divided by the SD over all pixels from the last dynamic frame  $t_{\text{noise}}$  (noise only) of the reconstruction without regularization  $\hat{\rho}_m$ . Metabolic SNR time curves were extracted as the average signal over all pixels of the left ventricular blood pool (pyruvate and pyruvate hydrate) and myocardium (lactate, alanine, and bicarbonate), respectively ( $V_{\text{ROI}}$ ):

$$\text{image SNR}_m(v, t_d) = \frac{|\rho_m(v, t_d)|}{\text{SD}(\text{Re}\{\hat{\rho}_m(v, t_{\text{noise}})\})}$$

$$\text{metabolic SNR}_m(t_d) = \frac{1}{|V_{\text{ROI}}|} \sum_{v \in V_{\text{ROI}}} \text{SNR}_m(v, t_d). \quad (16)$$

Segmentation of the left ventricular blood pool and myocardium was performed manually on a  $^1\text{H}$  anatomical reference scan. The AUC was calculated by signal integration of the baseline-corrected left ventricular pyruvate SNR over peak dynamic scan time.

In addition to metabolic imaging,  $^1\text{H}$  field maps for off-resonance correction were obtained using multi-echo acquisition,<sup>10</sup> and anatomical reference 2D cine cardiac images were acquired using a cardiac gated balanced steady-state free precession gradient echo sequence.<sup>10</sup>

## 4 | RESULTS

### 4.1 | Q-ratio measurements

In accordance with the theory, the Q-ratios of the 32 MHz coil were higher for all subject loads and coil-subject distances compared to the 16 MHz coil, and the Q-ratios decreased with increasing distance of the coil to the subject, asymptotically approaching a ratio of 1, i.e.  $Q_l = Q_u$  (Figure 2).

For both humans and pigs, the measured Q-ratio at minimum coil-subject distance (5 mm) was larger than 4 for both resonance frequencies, and thus, sample noise

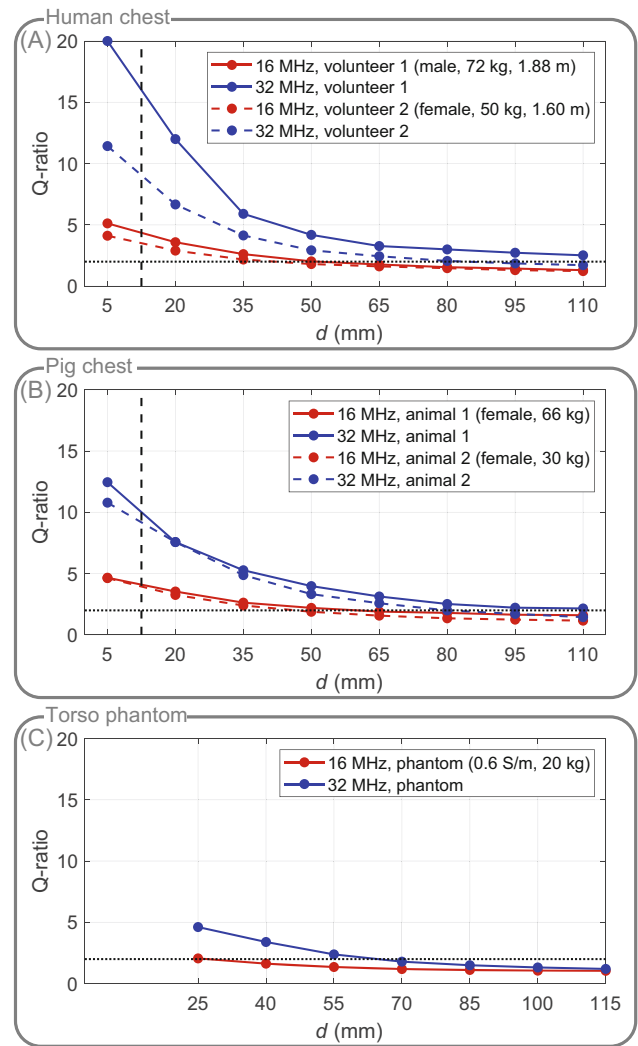


FIGURE 2 Experimentally determined Q-ratios of a 16 MHz (red) and 32 MHz (blue) single-loop coil with 10 cm radius on a human chest (A), porcine chest (B) and torso phantom (C) as a function of coil-subject distance  $d$ . Q-ratios greater than two (black dotted line) characterize higher contribution of sample versus coil noise. For in vivo suitable coils, the realistic minimum coil-subject distance is approximately 12.5 mm (black dashed line) due to padding and patient protection. The torso phantom has a minimum coil-subject distance of 25 mm due to its acrylic wall. Abbreviation: Q-ratio, quality factor ratio

exceeds coil noise. However, considering padding and patient protection results in a minimum distance for typical in vivo coils of approximately 10-15 mm. Hence, at a realistic coil-subject distance of 12.5 mm (interpolated), the experimentally determined Q-ratios were 3.5 or higher for in vivo loads. Loading with the torso phantom has a larger effective distance due to its acrylic wall, resulting in a maximum Q-ratio of 2.1 for the 16 MHz coil.

To determine the expected SNR scaling between different field strengths for a given Q-ratio, Equation 8 can be



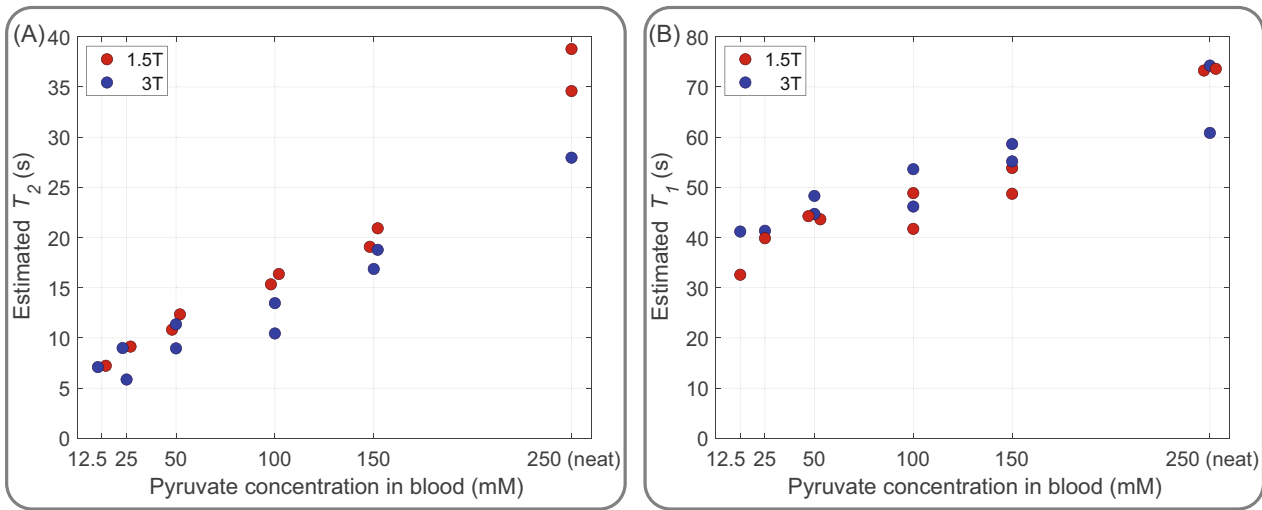


FIGURE 3 In vitro measured  $T_2$  (A) and  $T_1$  (B) values for different concentrations of pyruvate in blood at 1.5T (red) and 3T (blue).  $N = 2$  measurements were conducted per concentration per field strength

rewritten according to:

$$\text{SNR} \propto \frac{\omega^{3/4}}{\sqrt{Q_{\text{ratio}} \cdot \text{BW}}} \quad (17)$$

Using the experimentally determined Q-ratios at a coil-subject distance of 12.5 mm together with a constant acquisition bandwidth gives an expected 1.5T-to-3T SNR ratio of 1.14 (volunteer 1), 0.95 (volunteer 2), 0.93 (animal 1), and 0.91 (animal 2). Thus, for in vivo loads and realistic coil-subject distance, the examined coils attain an SNR ratio between 1.5T and 3T of approximately 1, and hence validate the assumption of sample noise dominance which allows for SNR scaling with  $\text{BW}^{-1/2}$  according to Equation 10.

S11 measurements performed along with the S21-based Q-ratio measurements (Supporting Information Figure S4) can be found in Supporting Information Figure S5.

## 4.2 | Relaxometry experiments in vitro

As expected, relaxometry measurements for pyruvate-blood concentrations between 12.5 mM and 250 mM (neat) yielded longer  $T_2$  values and shorter  $T_1$  values at 1.5T compared to 3T as depicted in Figure 3. The relative differences between relaxation times at 1.5T compared to 3T across all pyruvate concentrations in blood average  $\Delta T_2 = (19.2 \pm 12)\%$  and  $\Delta T_1 = (9.6 \pm 6.0)\%$ .

Due to the reduced amount of blood relative to pyruvate, and hence, reduced exposure to paramagnetic iron, both  $T_2$  and  $T_1$  relaxation parameters increase

for higher pyruvate-blood concentrations at both field strengths.

The estimated transverse relaxation times  $T_2$  are between 6 and 39 s, and hence, even for low concentrations of pyruvate in blood still relatively long. Assuming field inhomogeneities of  $(\gamma/2\pi)\Delta B_0 = 1$  ppm, yields according to Equation (12) for a realistic in vivo pyruvate-blood concentration of 12.5 mM ( $T_2^{1.5T} = 7.2$  s,  $T_2^{3T} = 7.1$  s) a  $T_2^*$  scaling of 1.9915 between 1.5T and 3T which deviates less than 0.5% from the theoretical scaling of  $T_2^{*1.5T/3T} \propto 1/(\omega^{1.5T/3T}) = 2$ . Based on that, the results verify Equation (12), and by exploiting this longer  $T_2^*$  at lower fields, the acquisition bandwidth can be adapted proportionally to  $\omega$  to increase SNR (Equation 13) without increasing field inhomogeneity effects.

Using the two-stage bolus timing model (Figure S6) together with the measured  $T_1$  values from Figure 3B, yields the  $T_1$  relaxation-induced SNR loss at 1.5T and 3T as reported in Table S1. The average SNR gain across all measured pyruvate-blood concentrations at 3T compared to 1.5T solely due to longer  $T_1$ , amounts to a negligible  $(2.0 \pm 2.2)$  percentage points, and therefore,  $T_1$  relaxation can be neglected in the theoretical SNR predictions for the field comparison.

## 4.3 | Computer simulations

As demonstrated in Figure 4A–C on the left, simulations of theoretical noise contributions suggest that small coils with 2.5 cm radius are coil noise-dominated for field strengths up to  $B_0 \leq 2.5$  T, while increasing the coil radius to 10 cm results in sample noise dominance for

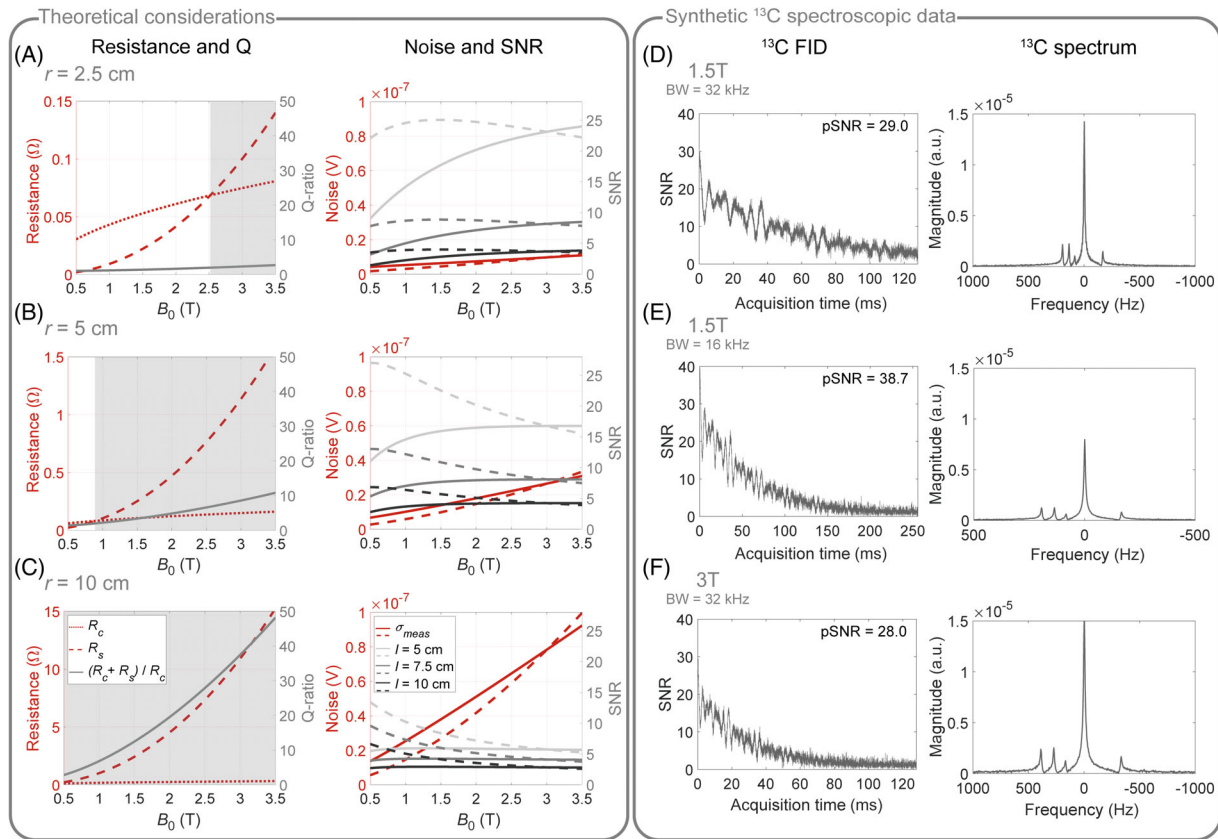


**FIGURE 4** Simulation-based field comparison. (A–C) Simulated noise and signal-to-noise ratio (SNR) behavior as a function of field strength  $B_0$  for different coil radii  $r$ . Left: Absolute contributions of coil resistance  $R_c$  (dotted red) and sample resistance  $R_s$  (dashed red) to total noise, and Q-ratio (solid gray) as a function of field strength. The sample noise-dominated regime ( $Q_{ratio} > 2 \Leftrightarrow R_s > R_c$ ) is shaded in gray. Right: Absolute noise levels (red) and intrinsically achievable SNR for different object depths  $l$  (gray) as a function of field strength. Field-dependent noise and SNR behavior are shown for fixed (solid lines) and adaptive (dashed lines) acquisition bandwidths. (D–F) Simulated FIDs and spectra of hyperpolarized [ $^{13}\text{C}$ ]pyruvate with downstream metabolites lactate, pyruvate hydrate, alanine, and bicarbonate, centered around pyruvate (0 Hz). Simulated spectral SNR behavior at 1.5T compared to 3T is demonstrated for fixed (D F) and adaptive (E) acquisition bandwidths. Abbreviations: BW, bandwidth; FID, free induction decay; Q-ratio, quality factor ratio; pSNR, peak SNR; SNR, signal-to-noise ratio

the clinically relevant range of field strengths  $0.5\text{T} \leq B_0 \leq 3.5\text{T}$ . For body imaging, in particular for cardiac applications, typically coils with large radii are used, and hence, sample noise exceeds coil noise. However, in larger coils, the absolute noise voltages are in general higher due to the increased electrical- and sample-induced noise seen by the coil, and therefore, the optimal coil size has to consider also the depth of the target organ, which is examined in Figure 4A–C on the right. In case of fixed acquisition bandwidth, the SNR penalty at 1.5T compared to 3T is less than 5% for a coil with 5 cm radius although sample and coil noise are of similar order at 1.5T. While the SNR penalty increases to 23% for small coils with 2.5 cm radius, the SNR is about the same at both field strengths for larger coils with 10 cm radius. For adaptive acquisition bandwidth, SNR is comparable between 1.5T and 3T even for small coil radii of 2.5 cm, and increases up to 46% SNR gain at 1.5T compared to 3T for coils with 10 cm radius.

Nevertheless, the overall noise  $\sigma_{meas}$  for a 10 cm coil is about eight times (3T) and six times (1.5T) higher than for a 2.5-cm coil.

As illustrated in Figure 4D–F, exemplary simulated  $^{13}\text{C}$  spectroscopic data at 1.5T and 3T demonstrate that SNR is comparable between 1.5T and 3T at identical acquisition bandwidths (D F). Comparing both spectra illustrates the reduced spectral span of the metabolites at 1.5T compared to 3T, which, together with the twice longer  $T_2^*$  at 1.5T, can be utilized to reduce the acquisition bandwidth by up to a factor of two (E) in order to effectively increase SNR by  $\sqrt{2} \approx 1.4$  at 1.5T versus 3T.

#### 4.4 | Thermal phantom experiments

As no hyperpolarization was used for the thermal  $^{13}\text{C}$  urea torso phantom, SNR at 1.5T is expected to be half that of

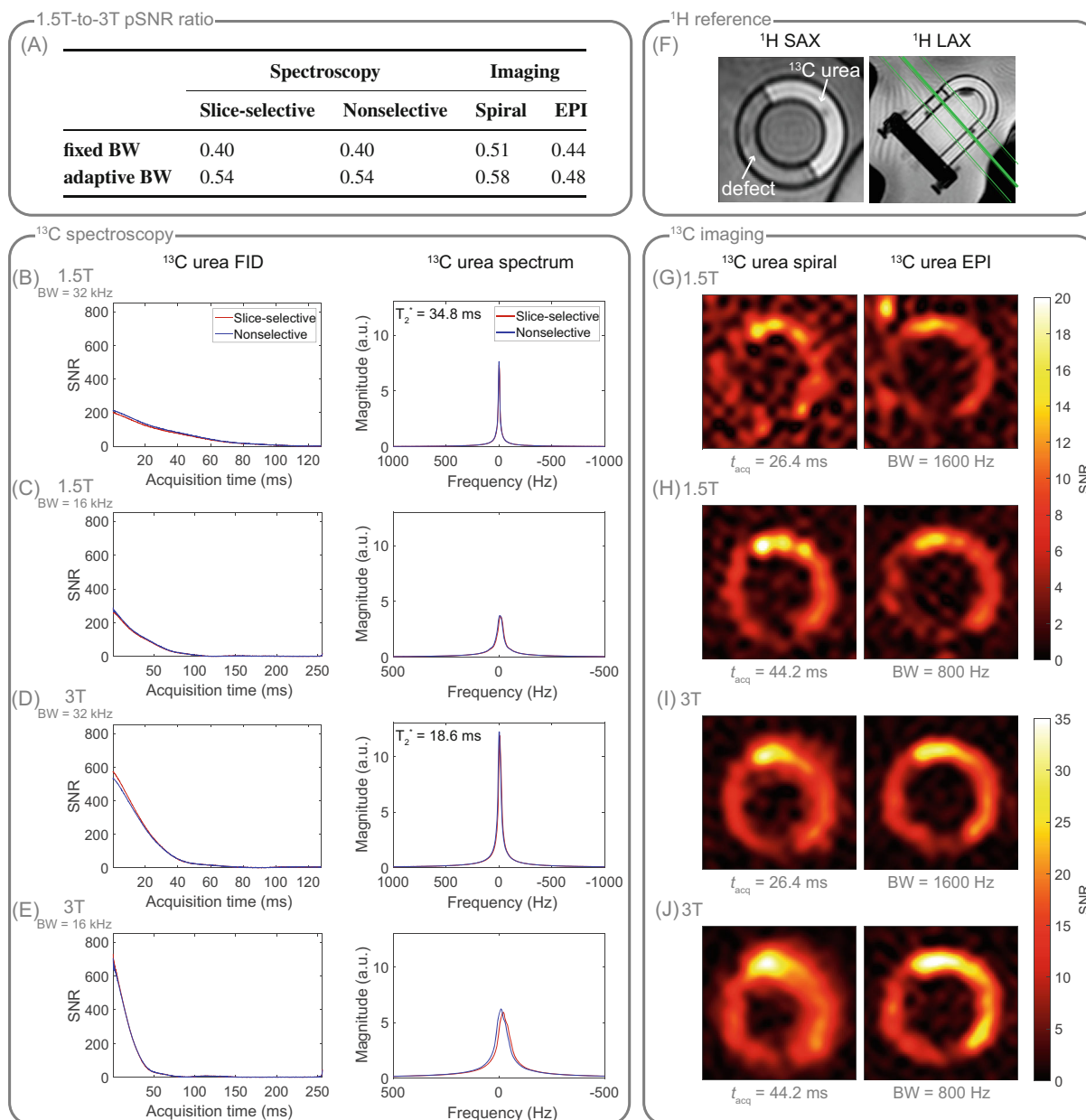


**FIGURE 5** Thermal <sup>13</sup>C urea phantom data at 1.5T and 3T. (A) Signal-to-noise ratio (SNR) ratios between 1.5T and 3T ( $pSNR^{1.5T}/pSNR^{3T}$ ) for thermal <sup>13</sup>C urea spectroscopy and imaging with and without adaptively changing the acquisition bandwidth. (B–E) Slice- (red) and nonselective (blue) spectroscopic data in time (FID) and frequency (spectrum) domain with fixed (B,D) and retrospectively reduced (C,E) acquisition bandwidth. Spectra are averaged over 128 signals. (G–J) Spiral and EPI images in short-axis view acquired with full (G,I) and reduced (H,J) acquisition bandwidth. Images are averaged over 128 signals. As illustrated in the <sup>1</sup>H reference scan (F), the left half of the myocardial compartment contains a defect area ( $H_2O$ +sodium chloride+gadolinium) that extends over two third of the <sup>13</sup>C image slice, resulting in reduced signal intensity. Abbreviations: BW, bandwidth; EPI, echo-planar imaging; FID, free induction decay; LAX, long-axis; pSNR, peak SNR; SAX, short-axis; SNR, signal-to-noise ratio

3T for fixed acquisition bandwidth. While spiral imaging yielded the expected SNR ratio of 0.5, spectral and EPI SNR ratios deviated about 20% and 12% to the disadvantage of 1.5T, respectively (Figure 5A).

For adapting the acquisition bandwidth by a factor of  $BW^{1.5T/3T}$ , SNR is expected to scale with  $\omega^{1.5T/3T}/\sqrt{BW^{1.5T/3T}} = 0.5/\sqrt{BW^{1.5T/3T}}$  according to

Equation (10) at thermal polarization. For the spectroscopic data, retrospectively reducing the bandwidth at 1.5T by a factor of two, yielded the expected SNR improvement of approximately  $\sqrt{2} \approx 1.4$  (Figure 5A–E). For spiral imaging, the acquisition windows of the low- and high-bandwidth images were 44.2 and 26.4 ms, respectively, resulting in a bandwidth scaling of  $BW^{1.5T/3T} = 0.6$ ,

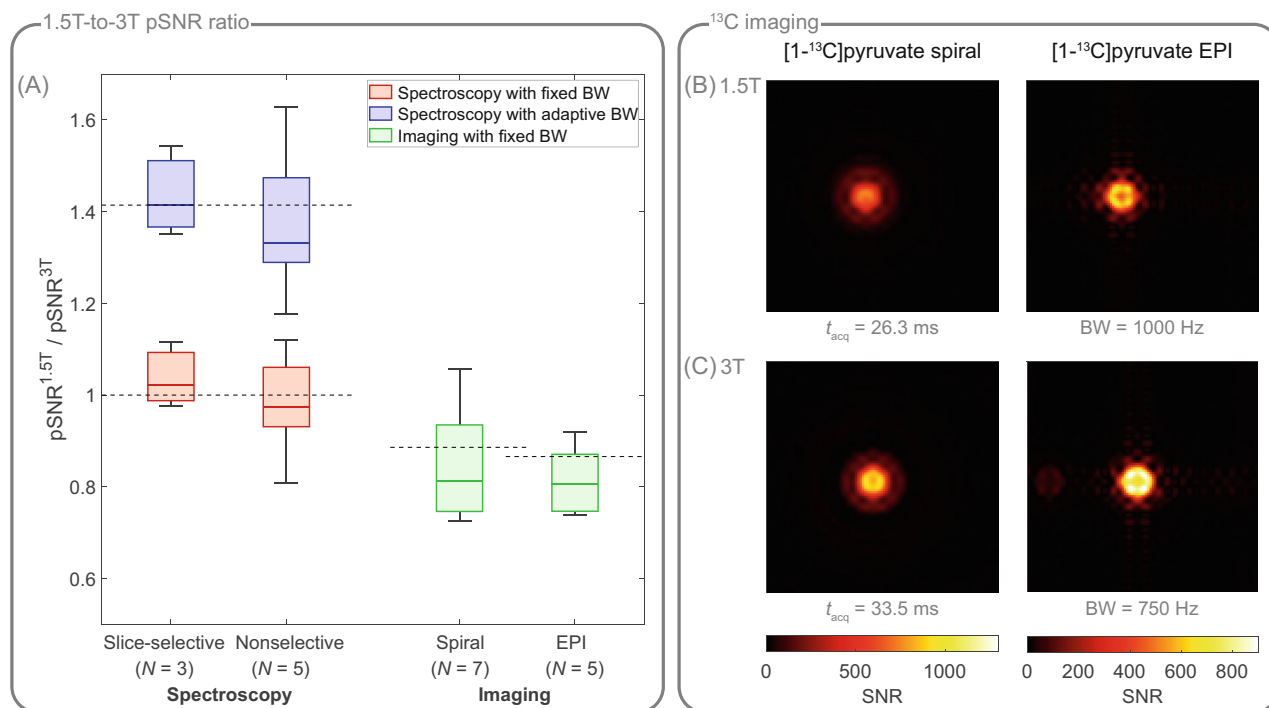


**FIGURE 6** In vitro hyperpolarized [1-<sup>13</sup>C]pyruvate data at 1.5T and 3T. (A) SNR ratios between 1.5T and 3T for slice- and nonselective spectroscopy using fixed (red) and retrospectively reduced (blue) acquisition bandwidth, as well as for spiral and EPI readouts (green). The distribution of SNR ratios is shown for *N* measurements, and the expected theoretical SNR ratios are indicated by the black dotted lines. Based on acquisition bandwidths at 1.5T and 3T, these expected SNR ratios are 0.89 / 0.87 for spiral / EPI readouts. (B,C) Exemplary spiral and EPI images at 1.5T (B) and 3T (C). In the EPI images, the pyruvate signal is seen in the center, while the low-intensity pyruvate hydrate signal is shifted to the left. Abbreviations: BW, bandwidth; EPI, echo-planar imaging; pSNR, peak SNR; SNR, signal-to-noise ratio

and thus in an SNR ratio of  $0.5/\sqrt{0.6} \approx 0.65$  between 1.5T and 3T, which is verified by the data. In EPI, the readout does not start in k-space center, and hence, reducing the acquisition bandwidth by half does not behave as predicted but still improves SNR by 10%.

Spiral and EPI images (Figure 5G–J) demonstrate that reducing the acquisition bandwidth generally improves SNR, even at 3T, but at the cost of increased field inhomogeneity effects like blurring (spiral) and stretching (EPI), as well as reduced effective spatial resolution (*H* / *J* versus *G* / *I*). In general, blurring is noticeably reduced at 1.5T compared to 3T, even for low acquisition bandwidth at 1.5T (*H*) and high acquisition bandwidth at 3T (*I*). Reducing the acquisition bandwidth at 1.5T visibly increases SNR compared to the higher bandwidth acquisition without severely suffering from blurring or stretching, respectively (*H* vs. *G*), whereas at 3T, reducing the bandwidth qualitatively leads to more blurring and stretching, respectively, but less SNR improvement (*J* vs. *I*). The optimal acquisition bandwidth, which maximizes SNR while retaining spatial resolution, is largely dependent on  $T_2^*$ , and therefore, longer readouts are generally favorable at 1.5T.

### 4.5 | Hyperpolarized in vitro experiments

Using hyperpolarized [1-<sup>13</sup>C]pyruvate spectroscopy in vitro, for identical acquisition bandwidths, the ratio of the spectroscopic SNR obtained at 1.5T and 3T amounts to  $1.04 \pm 0.07$  (slice-selective) /  $0.98 \pm 0.11$  (nonselective), and thus agrees with the expected theoretical SNR ratio of 1 (Figure 6A). Retrospectively reducing the bandwidth by a factor of two at 1.5T allows to increase SNR, resulting in a 1.5T-to-3T SNR ratio of  $1.44 \pm 0.10$  (slice-selective) /  $1.38 \pm 0.17$  (nonselective), which matches the expected SNR ratio of  $\sqrt{2} \approx 1.4$ .

For spiral and EPI images (Figure 6A–C), the SNR ratio between 1.5T and 3T amounts to  $0.85 \pm 0.12$  and  $0.81 \pm 0.08$ , respectively. Due to different gradient hardware at 1.5T and 3T, acquisition bandwidths varied between field strengths (Table 1), resulting in a bandwidth scaling of  $BW^{1.5T/3T} = 1.27$  (spiral) / 1.33 (EPI), and thus in an expected SNR ratio of  $1.27^{-0.5} \approx 0.89$  (spiral) /  $1.33^{-0.5} \approx 0.87$  (EPI) between 1.5T and 3T, which deviates 5% (spiral) / 7% (EPI) from the experimentally determined SNR ratio.

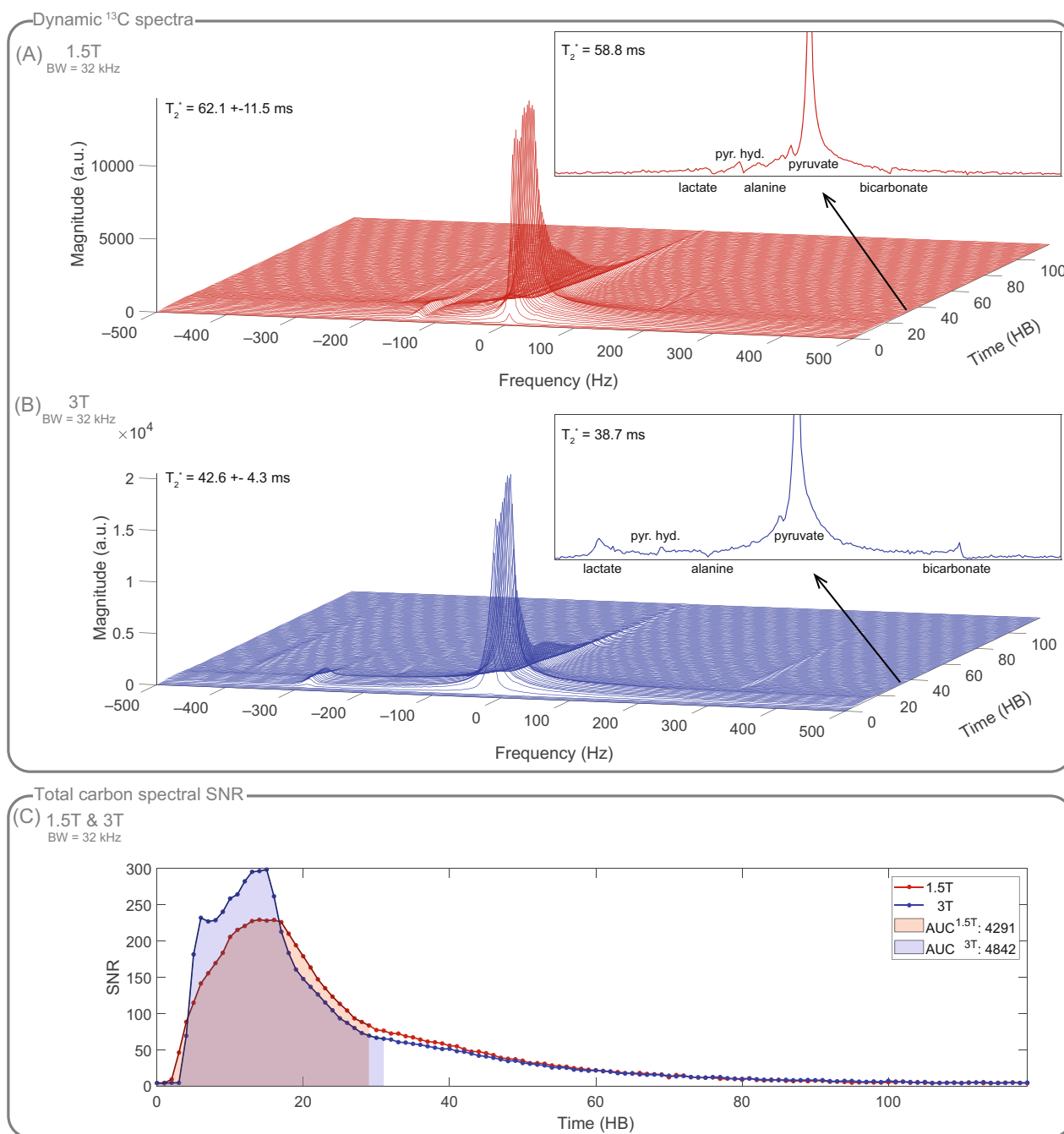


**FIGURE 7** In vivo dynamic cardiac spectroscopy after hyperpolarized  $[1-^{13}\text{C}]$ pyruvate injection in different pigs at 1.5T (red) and 3T (blue). (A-B) Metabolic spectra of pyruvate and its downstream metabolites lactate, pyruvate hydrate, alanine, and bicarbonate over dynamic scan time and at myocardial peak dynamic acquired at 1.5T (A) and 3T (B) with identical bandwidths. (C) Dynamic total carbon SNR derived from  $[1-^{13}\text{C}]$ pyruvate resonances on both field strengths. The AUCs (from the beginning until twice the time-to-peak of the total carbon signal) used for SNR comparison between field strengths are indicated by the shaded regions. Abbreviations: SNR, signal-to-noise ratio; BW, bandwidth; HB, heartbeat; AUC, area under the curve

#### 4.6 | Hyperpolarized in vivo experiments

The following presented in vivo data (Figures 7 and 8) were acquired at 1.5T and 3T in two different pigs (30 kg at 1.5T and 56.5 kg at 3T).

In vivo dynamic cardiac spectroscopy of hyperpolarized  $[1-^{13}\text{C}]$ pyruvate and its downstream metabolites at 1.5T and 3T with fixed acquisition bandwidth yielded a 1.5T-to-3T SNR ratio of 0.89 based on the AUCs of the total carbon SNRs (Figure 7).

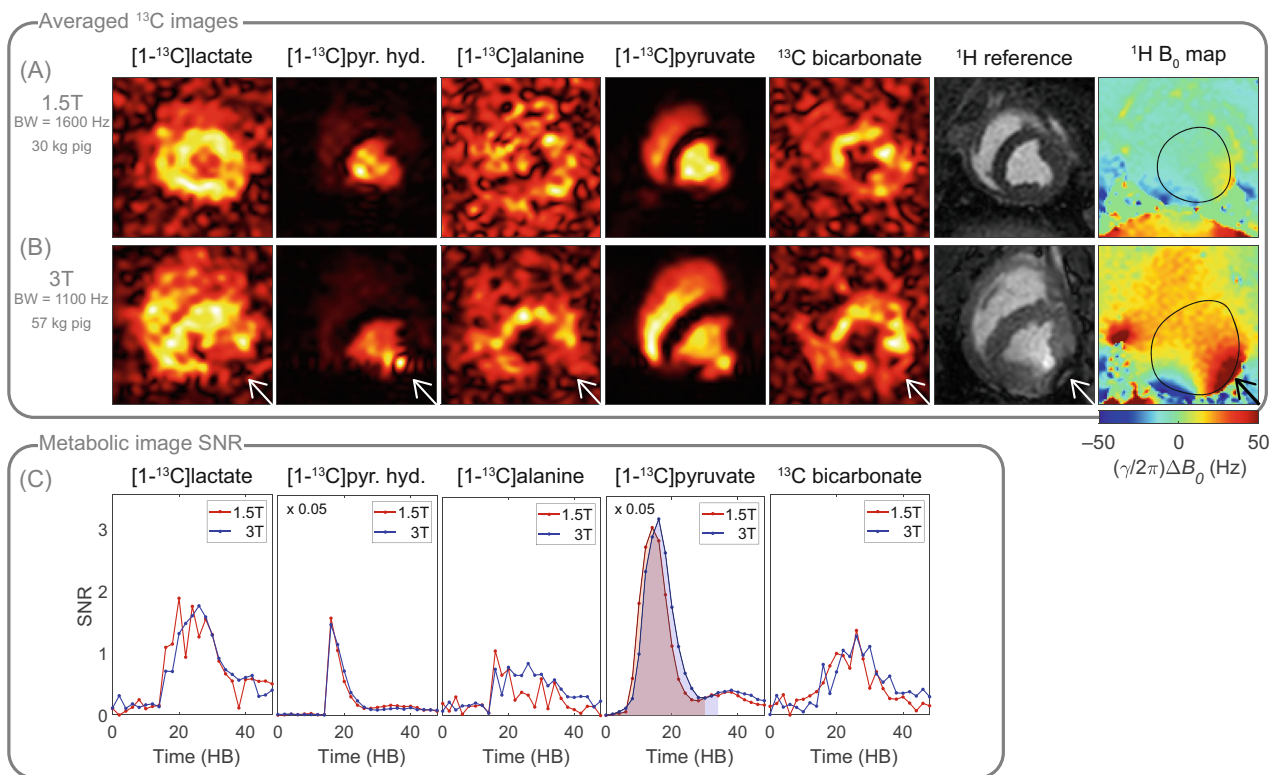


**FIGURE 8** In vivo dynamic cardiac EPI data of hyperpolarized  $[1-^{13}\text{C}]$ pyruvate and its downstream metabolites lactate, pyruvate hydrate, alanine, and bicarbonate acquired in different pigs at 1.5T and 3T. (A–B) Metabolic  $^{13}\text{C}$  images (averaged over ten dynamics around peak signal) with corresponding  $^1\text{H}$  anatomical reference cine image and  $B_0$  map at 1.5T (A) and 3T (B).  $B_0$  off-resonance effects due to field inhomogeneities (white and black arrows, respectively) are noticeably reduced at 1.5T. (C) SNR time curves of the individual metabolites at 1.5T (red) and 3T (blue). For pyruvate, the AUCs (from the beginning until twice the time-to-peak of the pyruvate signal) are indicated by the shaded regions. Abbreviations: SNR, signal-to-noise ratio; EPI, echo-planar imaging; HB, heartbeat; AUC, area under the curve

For dynamic EPI of hyperpolarized  $[1-^{13}\text{C}]$ pyruvate and its downstream metabolites at 1.5T and 3T, SNR time curves of the individual metabolites, and the 1.5T-to-3T pyruvate AUC ratio of 0.9 confirm that comparable SNR was achieved between field strengths (Figure 8) despite the lower EPI bandwidth at 3T (Table 1) due to different gradient hardware, leading to a bandwidth scaling of  $\text{BW}^{1.5\text{T}/3\text{T}} = 1.45$ , and hence in an expected SNR ratio of  $1.45^{-0.5} \approx 0.83$  between 1.5T and 3T. The typical off-resonance effects in the inferior region of the myocardium are significantly reduced at 1.5T, both in metabolic  $^{13}\text{C}$  images and  $^1\text{H}$  cine images. Improved shimming is apparent in the corresponding  $^1\text{H}$  field maps. Further in vivo data acquired at 1.5T can be found in Figure S8.

## 5 | DISCUSSION

In this work, the potential of hyperpolarized  $^{13}\text{C}$  MRS and MRI at 1.5T compared to 3T has been demonstrated in silico, in vitro, and in vivo.

Theoretical considerations combined with simulations have shown that the SNR of hyperpolarized MR signals at identical acquisition bandwidths is independent of the field strength for typical coil setups. By adaptively changing the acquisition bandwidth proportional to the static magnetic field, motivated by reduced spectral span and longer  $T_2^*$  at lower field strengths, we predicted that net SNR gains of up to 40% at 1.5T compared to 3T can be achieved.

Simulation results are subject to assumptions, such as sample noise dominance, long  $T_2$ , and comparable  $T_1$  relaxation among field strengths, which were validated based on experimentally determined Q-ratios and relaxation parameters, respectively. Scanner system-related noise contributions, for example, from receive chain electronics or low-noise amplifiers LNAs,<sup>31</sup> were considered field-independent and therefore neglected in the theoretical SNR considerations. While typical hardware is capable to operate at frequencies down to 10 MHz, this frequency range is not a focus during system design, and hence the filter characteristics of the RF cabin and receive chain might need to be adjusted and optimized. Moreover, SNR

simulations were based on a signal point source rather than a realistic target shape. Considering not only the depth but also the shape of the target would underline the requirement for larger coils, and hence favorable SNR scaling in many in vivo applications. The remaining uncertainties caused by the simplifications are not believed to substantially affect the conclusions drawn herein.

In addition to the simulations, a thorough field comparison between 1.5T and 3T was performed on thermal phantom and hyperpolarized in vitro  $^{13}\text{C}$  data. It is important to note that in vitro experiments were conducted under identical conditions, namely coil design, transmit–receive RF chains including integrated preamplifiers, acquisition sequence, phantom design, as well as same hyperpolarized  $[1-^{13}\text{C}]$ pyruvate solution and equal duration from dissolution to scan time. Spectroscopy and imaging results verified that for thermal polarization, SNR at 1.5T is about half the SNR at 3T, while hyperpolarization allowed to mostly retain SNR when going from 3T to 1.5T. Reducing the acquisition bandwidth allowed to increase SNR at 1.5T in both cases as expected. All results were within a maximum error margin of 20% for thermal and 7% for hyperpolarized  $^{13}\text{C}$  MR.

For the phantom and in vitro SNR field comparison using spiral imaging, the increased point spread function widening at 3T due to stronger field inhomogeneities, and the associated lower resolution and hence increased SNR, have not been considered. Consequently, for spiral imaging, the expected 1.5T-to-3T SNR ratio is effectively lower.

Grid-like artifacts were observed in the EPI images of the thermal phantom after averaging (Figure S7). Albeit these artifacts appear at both field strengths, they are less severe at 3T, and therefore, EPI SNR scaling for the thermal phantom might have been compromised to the disadvantage of 1.5T.

Finally, in vivo feasibility of hyperpolarized  $[1-^{13}\text{C}]$ pyruvate metabolic spectroscopy and imaging at 1.5T was demonstrated in the pig heart. Both spectroscopy and imaging data showed comparable SNR between 1.5T and 3T, while  $B_0$  artifacts were noticeably reduced at 1.5T, which supports the elaborated hypotheses. However, in contrast to the presented in vitro experiments, in vivo data were not acquired exclusively under identical conditions due to experimental complexity. Data were obtained in different pigs using equally prepared hyperpolarized pyruvate solutions. Nevertheless, polarization duration, and time from dissolution to injection were comparable, and identical coils and sequences were used for data acquisition. For a fair comparison, data with similar injection bolus timing and duration were chosen, however, the diversity of image qualities (Figure S8) suggests that intersubject variability caused by subject size, weight,

metabolic state, and heart rate, impact SNR to a large degree. Hence, the in vivo data presented in Figures 7 and 8 are solely representing exemplary data quality at 1.5T. In addition to intersubject variability between animals, intrasubject variability caused by metabolic condition, positioning, preparation, and different hyperpolarized dissolutions impair direct comparison of hyperpolarized metabolic imaging for consecutive measurements in one animal in two different scanners. Therefore, a conclusive in vivo field comparison is not feasible in a direct experimental implementation, but requires a high sample size to be statistically meaningful, which is not only demanding but also ethically controversial.

In summary, as predicted theoretically and by simulations, our hyperpolarized in vitro and in vivo data showed comparable SNR between 1.5T and 3T without bandwidth scaling while reducing field inhomogeneity effects, which is consistent with previous work of hyperpolarized  $^{129}\text{Xe}$  and  $^3\text{He}$  lung MRI comparing 1.5T and 3T<sup>5,7,32</sup> as well as field strengths  $\leq 1.5\text{T}$ .<sup>6</sup>

A major limitation of the in vitro and in vivo measurements is that the imaging bandwidths were not the same at 1.5T and 3T (Table 1) due to different gradient hardware settings. More precisely, the bandwidth at 3T was lower compared to 1.5T which improves SNR scaling to the advantage of 3T so that we observed lower SNR at 1.5T than at 3T although equal SNR was expected. Nevertheless, we compensated for that during the evaluation as explained in the corresponding Results sections.

Reducing field strength in hyperpolarized MRI offers two advantages that need to be traded off against each other: On the one hand, if acquisition bandwidth is kept constant, which retains SNR, unwanted field inhomogeneity effects like blurring, geometrical distortions, or signal dephasing are reduced. On the other hand, lowering the acquisition bandwidth with reduced field strength can increase SNR at the cost of reduced spectral separability and similar  $B_0$  artifacts. As shimming is generally more robust at lower field,  $B_0$  effects are still partly reduced. This trade-off has to be balanced for each experiment individually depending on the applied acquisition strategy. Furthermore, reducing bandwidth for readouts which do not start in the k-space center, such as EPI, will prolong echo times, limiting the net SNR gain in practice. Consequently, the effective impact on image quality with respect to SNR and  $B_0$  effects is subject to thorough sequence design on a per-case basis.

In metabolic imaging, spectral separation of metabolites either by spectrally selective excitation,<sup>33–35</sup> or by echo shift encoding<sup>36,37</sup> poses a challenge. At lower fields, the reduced chemical shift leads to longer echo times which partly counteract the longer  $T_2^*$ , thus limiting the available SNR gain. In particular selective excitation of

[1-<sup>13</sup>C]pyruvate and its downstream metabolites at 1.5T is very challenging due to the small chemical shift of ~50 Hz between pyruvate hydrate and lactate/alanine, respectively, which imposes a minimum total RF pulse duration. MRS of hyperpolarized <sup>13</sup>C pyruvate on the other hand is generally less limited by the lower frequency separation of peaks at lower fields, and hence, fully benefits from longer T<sub>2</sub>\* at 1.5T compared to 3T. Nevertheless, the resulting constraints of reduced spectral separation on the acquisition heavily depend on the hyperpolarized substrate and hence chemical shifts of the peaks.

While this work is based on large single- or dual-loop coils ( $r \approx 10$  cm), often coil arrays of multiple smaller loops are used to improve the detection sensitivity without limiting the field of view,<sup>21</sup> or for making use of parallel imaging.<sup>38</sup> For hyperpolarized <sup>13</sup>C body imaging, the individual loops of such arrays typically have radii around 5 cm<sup>38,39</sup> (or corresponding rectangular sizes with similar areas<sup>40</sup>), for which sample noise still slightly exceeds coil noise at 1.5T (Figure 4). However, our Q-ratio measurements showed that the 16 MHz single-loop coil with 10 cm radius is already at the limit and hence coil arrays with small loops might be coil noise-dominated and therefore not beneficial at lower fields.

Especially for cardiac applications, where large coil diameters are common, hyperpolarized MRI at 1.5T is a promising alternative to 3T as it showed less off-resonance-related artifacts and dephasing near venous vessels and lung spaces. Furthermore, ECG triggering is more reliable at 1.5T, and thus the need of repositioning the ECG electrodes or switching to peripheral pulse oximetry devices due to poor ECG signals, as often necessary at 3T, can be avoided. Lastly, hyperpolarized MR at 1.5T offers the possibility to integrate <sup>13</sup>C metabolic imaging into the clinical workflow facilitating multi-modal cardiovascular MR.

## 6 | CONCLUSION

We have demonstrated that hyperpolarized <sup>13</sup>C MRS and MRI are not only feasible but also suitable at clinical 1.5T setups offering comparable or even better SNR compared to 3T. In particular for cardiac metabolic imaging, hyperpolarized MRI at 1.5T proved to be capable of enhancing image quality by increasing SNR or by reducing B<sub>0</sub>-induced artifacts when compared to 3T. Consequently, hyperpolarized <sup>13</sup>C MRI at 1.5T allows addressing challenges with respect to SNR and off-resonance effects, which are currently seen in hyperpolarized metabolic imaging at 3T.

## ACKNOWLEDGMENTS

The authors would like to acknowledge Miriam Weisskopf and Christian Stoeck for animal handling and care.

## DATA AVAILABILITY STATEMENT

The simulation code of Section 3.3 is publicly available at [https://gitlab.ethz.ch/ibt-cmr-public/13c\\_field\\_comparison\\_simulation.git](https://gitlab.ethz.ch/ibt-cmr-public/13c_field_comparison_simulation.git).


## ORCID

Julia Traechtler  <https://orcid.org/0000-0001-6868-6262>

Maximilian Fuetterer  <https://orcid.org/0000-0002-7456-1180>

Mohammed M. Albannay  <https://orcid.org/0000-0002-6635-8844>

Tobias Hoh  <https://orcid.org/0000-0002-1391-6347>

Sebastian Kozerke  <https://orcid.org/0000-0003-3725-8884>

## TWITTER

Sebastian Kozerke  @CMR\_Zurich

## REFERENCES

1. Wang ZJ, Ohliger MA, Larson PEZ, et al. Hyperpolarized <sup>13</sup>C MRI: state of the art and future directions. *Radiology*. 2019;291:273-284.
2. Wei Y, Yang C, Jiang H, et al. Multi-nuclear magnetic resonance spectroscopy: state of the art and future directions. *Insights Imaging*. 2022;13:135.
3. Timm KN, Miller JJ, Henry JA, Tyler DJ. Cardiac applications of hyperpolarised magnetic resonance. *Progress Nucl Magnet Reson Spectrosc*. 2018;106-107:66-87.
4. Parra-Robles J, Cross AR, Santyr GE. Theoretical signal-to-noise ratio and spatial resolution dependence on the magnetic field strength for hyperpolarized noble gas magnetic resonance imaging of human lungs. *Med Phys*. 2005;32:221-229.
5. Deppe MH, Parra-Robles J, Ajraoui S, et al. Susceptibility effects in hyperpolarized <sup>3</sup>He lung MRI at 1.5T and 3T. *J Magnet Reson Imaging*. 2009;30:418-423.
6. Komlosi P, Altes TA, Qing K, et al. Signal-to-noise ratio, T<sub>2</sub>, and T<sub>2</sub>\* for hyperpolarized helium-3 MRI of the human lung at three magnetic field strengths. *Magnet Reson Med*. 2017;78:1458-1463.
7. Dominguez-Viqueira W, Ouriadov A, O'Halloran R, Fain SB, Santyr GE. Signal-to-noise ratio for hyperpolarized <sup>3</sup>He MR imaging of human lungs: a 1.5 T and 3 T comparison. *Magnet Reson Med*. 2011;66:1400-1404.
8. Wiens CN, Friesen-Waldner LJ, Wade TP, Sinclair KJ, McKenzie CA. Chemical shift encoded imaging of hyperpolarized <sup>13</sup>C pyruvate. *Magnet Reson Med*. 2015;74:1682-1689.
9. Geraghty BJ, Lau JYC, Chen AP, Cunningham CH. Dual-Echo EPI sequence for integrated distortion correction in 3D time-resolved hyperpolarized <sup>13</sup>C MRI. *Magnet Reson Med*. 2018;79:643-653.



10. Traechtler J, Vishnevskiy V, Fuetterer M, Kozerke S. Joint image and field map estimation for multi-echo hyperpolarized  $^{13}\text{C}$  metabolic imaging of the heart. *Magnet Reson Med.* 2021;86:258-276.
11. Miller JJ, Lau AZ, Tyler DJ. Susceptibility-induced distortion correction in hyperpolarized echo planar imaging. *Magnet Reson Med.* 2018;79:2135-2141.
12. Wang J, Wright AJ, Hu D, Hesketh R, Brindle KM. Single shot three-dimensional pulse sequence for hyperpolarized  $^{13}\text{C}$  MRI. *Magnet Reson Med.* 2017;77:740-752.
13. Reed GD, Ma J, Park JM, et al. Characterization and compensation of  $f_0$  inhomogeneity artifact in spiral hyperpolarized  $^{13}\text{C}$  imaging of the human heart. *Magnet Reson Med.* 2021;86:157-166.
14. Müller CA, Hundshammer C, Braeuer M, et al. Dynamic 2D and 3D mapping of hyperpolarized pyruvate to lactate conversion in vivo with efficient multi-echo balanced steady-state free precession at 3 T. *NMR Biomed.* 2020;33:e4291.
15. Perman WH, Bhattacharya P, Leupold J, et al. Fast volumetric spatial-spectral MR imaging of hyperpolarized  $^{13}\text{C}$ -labeled compounds using multiple echo 3D BSSFP. *Magnet Reson Imaging.* 2010;28:459-465.
16. Leupold J, Månsson S, Petersson JS, Hennig J, Wieben O. Fast multiecho balanced SSFP metabolite mapping of  $^1\text{H}$  and hyperpolarized  $^{13}\text{C}$  compounds. *Magnet Reson Mater Phys Biol Med.* 2009;22:251-256.
17. Krug JW, Rose G. Magneto-hydrodynamic distortions of the ECG in different MR scanner configurations. *2011 Comput Cardiol.* 2011;38:769-772.
18. Kramer CM, Barkhausen J, Bucciarelli-Ducci C, Flamm SD, Kim RJ, Nagel E. Standardized cardiovascular magnetic resonance imaging (CMR) protocols: 2020 update. *J Cardiovasc Magnet Reson.* 2020;22:17.
19. Brown RW, Cheng YCN, Haacke EM, Thompson MR, Venkatesan R. *Magnetic Resonance Imaging: Physical Principles and Sequence Design.* John Wiley & Sons; 2014.
20. Golman K, Petersson JS. Metabolic imaging and other applications of hyperpolarized  $^{13}\text{C}$ . *Acad Radiol.* 2006;13:932-942.
21. Frass-Kriegl R, Hosseinnzhadian S, Poirier-Quinot M, Laistler E, Ginefri JC. Multi-loop radio frequency coil elements for magnetic resonance imaging: theory, simulation, and experimental investigation. *Front Phys.* 2020;7:237.
22. Darrasse L, Ginefri JC. Perspectives with cryogenic RF probes in biomedical MRI. *Biochimie.* 2003;85:915-937.
23. Suits BH, Garroway AN, Miller JB. Surface and gradiometer coils near a conducting body: the lift-off effect. *J Magnet Reson.* 1998;135:373-379.
24. Sanchez-Heredia JD, Hansen ESS, Laustsen C, Zhurbenko V, Ardenkjær-Larsen JH. Low-noise active decoupling circuit and its application to  $^{13}\text{C}$  cryogenic RF coils at 3 T. *Tomography.* 2017;3:60-66.
25. Giovannetti G. Multiturn surface coil: theoretical considerations on unloaded to loaded Q ratio and SNR. *Concepts Magnet Reson B Magnet Reson Eng.* 2014;44:27-31.
26. Darrasse L, Kassab G. Quick measurement of NMR-coil sensitivity with a dual-loop probe. *Rev Sci Instr.* 1993;64:1841-1844.
27. Meiboom S, Gill D. Modified spin-echo method for measuring nuclear relaxation times. *Rev Sci Instr.* 1958;29:688-691.
28. Traechtler J, Fuetterer M, Hoh T, Albannay M, Dounas A, Kozerke S. On the impact of heart rate and relaxation on SNR of hyperpolarized  $^{13}\text{C}$  pyruvate metabolic imaging of the human heart. Proceedings of the 30th Annual Meeting of the ISMRM; 2022; London, England. Abstract 1070.
29. Matula RA. Electrical resistivity of copper, gold, palladium, and silver. *J Phys Chem Ref Data.* 1979;8:1147-1298.
30. Fuetterer M, Traechtler J, Busch J, et al. Hyperpolarized metabolic and parametric cardiovascular magnetic resonance imaging of longitudinal metabolic-structural changes in experimental chronic infarction. *JACC Cardiovasc Imaging.* 2022;15:2051-2064.
31. Kumar A, Edelstein WA, Bottomley PA. Noise figure limits for circular loop MR coils. *Magnet Reson Med.* 2009;61:1201-1209.
32. Xu X, Norquay G, Parnell SR, et al. Hyperpolarized  $^{129}\text{Xe}$  gas lung MRI-SNR and  $T_2^*$  comparisons at 1.5 T and 3 T. *Magnet Reson Med.* 2012;68:1900-1904.
33. Cunningham CH, Chen AP, Lustig M, et al. Pulse sequence for dynamic volumetric imaging of hyperpolarized metabolic products. *J Magnet Reson.* 2008;193:139-146.
34. Larson PE, Kerr AB, Chen AP, et al. Multiband excitation pulses for hyperpolarized  $^{13}\text{C}$  dynamic chemical-shift imaging. *J Magnet Reson.* 2008;194:121-127.
35. Lau AZ, Chen AP, Hurd RE, Cunningham CH. Spectral-spatial excitation for rapid imaging of DNP compounds. *NMR Biomed.* 2011;24:988-996.
36. Wiesinger F, Weidl E, Menzel MI, et al. IDEAL spiral CSI for dynamic metabolic MR imaging of hyperpolarized  $[1-^{13}\text{C}]$ pyruvate. *Magnet Reson Med.* 2012;68:8-16.
37. Sigfridsson A, Weiss K, Wissmann L, et al. Hybrid multiband excitation multiecho acquisition for hyperpolarized  $^{13}\text{C}$  spectroscopic imaging. *Magnet Reson Med.* 2015;73:1713-1717.
38. Sanchez-Heredia JD, Olin RB, Grist JT, et al. RF coil design for accurate parallel imaging on  $^{13}\text{C}$  MRSI using  $^{23}\text{Na}$  sensitivity profiles. *Magnet Reson Med.* 2022;88:1391-1405.
39. Fütterer MN. *Enhanced Spectroscopy and Hyperpolarized Perfusion MRI of the Heart.* PhD thesis, ETH Zurich; 2018.
40. Sánchez-Heredia JD, Olin RB, McLean MA, et al. Multi-site benchmarking of clinical  $^{13}\text{C}$  RF coils at 3T. *J Magnet Reson.* 2020;318:106798.

## SUPPORTING INFORMATION

Additional supporting information may be found in the online version of the article at the publisher's website.

### Appendix S1. Supporting tables and figures

**How to cite this article:** Traechtler J, Fuetterer M, Albannay MM, Hoh T, Kozerke S. Considerations for hyperpolarized  $^{13}\text{C}$  MR at reduced field: Comparing 1.5T versus 3T. *Magn Reson Med.* 2023;89:1945-1960. doi: 10.1002/mrm.29579